

# We are IntechOpen, the world's leading publisher of Open Access books Built by scientists, for scientists

6,900

Open access books available

185,000

International authors and editors

200M

Downloads

Our authors are among the

154

Countries delivered to

TOP 1%

most cited scientists

12.2%

Contributors from top 500 universities



WEB OF SCIENCE™

Selection of our books indexed in the Book Citation Index  
in Web of Science™ Core Collection (BKCI)

Interested in publishing with us?  
Contact [book.department@intechopen.com](mailto:book.department@intechopen.com)

Numbers displayed above are based on latest data collected.  
For more information visit [www.intechopen.com](http://www.intechopen.com)



# Fingerprint Spoof Detection Using Near Infrared Optical Analysis

Shoude Chang<sup>1</sup>, Kirill V. Larin<sup>2</sup>, Youxin Mao<sup>1</sup>,  
Costel Fluera<sup>1</sup> and Wahab Almuhtadi<sup>3</sup>

<sup>1</sup>*Institute for Microstructural Sciences, National Research Council Canada, Ottawa*

<sup>2</sup>*Department of Biomedical Engineering, University of Houston, Houston*

<sup>3</sup>*Algonquin College, Ottawa*

<sup>1,3</sup>*Canada*

<sup>2</sup>*USA*

## 1. Introduction

Fingerprints have been used for several centuries as a means of identifying individuals. Since every fingerprint is considered to be unique, fingerprint recognition is the most popular biometric identification method currently employed in such areas as law enforcement, financial transactions, access control, and information security. Fingerprints consist of ridges and furrows on the surface of a fingertip. The ridges are the raised portions of the fingerprint while the furrows are the spaces between the ridges. Recognition can be performed based on ridge ending and ridge bifurcation (Xiao & Raffat, 1990), tessellated invariant moment (Yang & Park, 2008), and image-based features (Nanni & Lumini, 2009). Since the ridges are created by nature, people may consider that stealing and duplicating a fingerprint is more difficult than stealing a password or token, but it turns out that it is not difficult to make an artifact to fool an automated fingerprint system. It has been reported that an automated fingerprint authentication system could be defeated either using “a combination of low cunning, cheap kitchen supplies and a digital camera” , or simply by creating false thumbprint images . These sensor-level attacks are called “spoofing” attacks in which an artifact containing a copy of the fingerprint traits of a legitimate enrolled user is used to fool a fingerprint system. The first step is to obtain the fingerprint of a legitimate user, which can be accomplished by lifting a latent print either with or without the co-operation of the fingerprint owner. Next, molding plastic and gelatin can be used to make “gummy fingers”. Finally, the resulting fake fingers can be used to fool the fingerprint sensor and attack the security system. The vulnerability to fake-finger attack has generated a wave of research concerned with adding “liveness detection” to improve system resistance to spoofing. Liveness detection is the ability to determine whether a biometric sample is being provided by a live human being rather than from a copy created using an artifact. The detection methods can be categorized into two groups: hardware-based and software-based. In hardware-based solutions, extra hardware must be integrated with biometric sensors to detect additional information such as heartbeat, temperature, and the tissue under the epidermis. For example, an extra sensor can be used to measure either blood flow or pulse

in the fingertip in order to identify a living finger, although there are several problems associated with this approach. Using heart rhythm as a biometric feature is unreliable, since a person's heartbeat can vary considerably and is affected by many different factors. Furthermore, the sensor can be easily spoofed by adding a pipe to the fake finger and pumping saltwater through the pipe to imitate blood flow. A second example of a hardware-based solution uses temperature as a liveness feature to distinguish a dummy finger from a real one. However, the temperature of the epidermis is about 8-10°C above the room temperature that is 18-20°C in an office environment. By using a silicone artificial fingerprint, the temperature only decreases by a maximum of 2°C (6-8°C), which is still in the working margins of the sensor. Another hardware-based detection method utilizes an optical sensor and multispectral imaging to capture the sub-surface of the skin to prevent spoofing. The fingerprint images are captured using different wavelengths of illumination to penetrate the skin to different depths, thereby obtaining multiple images of the surface and subsurface of the fingertip. Since these devices are more complex than conventional optical sensors, they are also more expensive.

On the other hand, software-based solutions focus on using the information captured from a standard fingerprint sensor, and liveness detection can be performed by simply modifying the algorithm to measure skin properties such as perspiration, elasticity, and deformation. The algorithms can be roughly divided into two groups based on whether they extract static or dynamic features: static approaches compare the features extracted from one or more fingerprint impressions, while dynamic methods analyze multiple frames of the same image captured over a certain time period. An early effort on software-based liveness detection used the perspiration pattern, which depends on a unique physiological feature of the skin – evaporation from the human body – to distinguish real fingers from artificial ones. Perspiration-based methods characterize and analyze the sweating pattern of live finger from two consecutive images captured over a period of a few seconds to detect the perspiration phenomenon. However, this approach is susceptible to a number of factors, such as the finger pressure applied, environmental moisture, and user cooperation. Another technique is based on the elastic deformation of the skin. When a finger touches a sensor, the elastic deformation will cause a distortion of the minutiae location. Because most of the materials used for making fake fingers are harder than human skin, the study showed that artificial fingers presented different deformations than the live ones. However, this approach performs poorly when the hardness of the fake finger is similar to that of live skin. The main advantages of software solutions are that no additional equipment needs to be integrated and there is less chance of revealing an individual's health status due to privacy concerns.

In order to take the advantages and avoid disadvantages of software-based and hardware-based methods, a combined software-hardware approach is presented to defeat fingerprint spoofing attack in this chapter. Two methods are presented based on analyzing different optical properties between human skin and artificial finger. The first method uses optical coherence tomography (OCT) technology and the second performs spectral analysis. Not only do both methods capture the ridge pattern appearing on the skin, but also measure the internal properties of the skin defined as internal biometrics to differentiate real and prosthetic fingers. This chapter is structured as follows: Section 2 introduces the layered structure of human skin and analyzes the skin's optical properties demonstrating its complexity, making it difficult to fake. Section 3 introduces OCT technology, presents a

concept of internal biometrics, and presents a solution to distinguish prosthetic and real fingers using internal biometrics measured with OCT. Section 4 investigates the differences of light reflection properties between prosthetic and real fingers, and presents an imaging system to explore the spectral features of prosthetic and real fingers. The experimental results, presented in Section 3 and Section 4, demonstrate the validity of OCT and spectral analysis as a software-hardware fingerprint anti-spoofing technique. Finally, a conclusion summarizes the main contributions of the work, discusses the technical challenges, and indicates the future research directions.

## 2. Optical properties of human skin

Since prosthetic and real fingers are often indistinguishable on the surface, it is necessary to study aspects of human skin, analyze its optical properties, and identify the features that make it difficult to replicate. In this section, we look at the multilayered skin structure of fingerprints. First, we introduce the major skin layers, and then analyze how they affect the skin's optical properties, such as scattering, absorption, and penetration depth, which will be used in performing near infrared (NIR) optical analysis to differentiate real and prosthetic fingers. For example, scattering and absorption are the two main physicochemical phenomena that occur with light inside the skin. A fake gelatin finger is a homogeneous medium that typically presents a significantly lower scattering profile than that of human skin.

The skin is the largest organ of the body and is composed of specialized epithelial and connective tissue cells. The skin has many important functions: it serves as a barrier to the environment as well as a channel for communication to the outside world; it protects the body from water loss and impact wounds; it uses specialized pigment cells to protect the body from ultraviolet radiation; and it helps to regulate body temperature and metabolism.

The skin is composed of several layers (Figure 1). The innermost layer contains subcutaneous fatty tissue with stores of adipose tissue. Above this is the dermis layer, which consists of connective tissue, blood vessels, nerve endings, hair follicles, and sweat and oil glands. The outermost layer of skin is called the epidermis.

The epidermis is mainly composed of keratinocytes, which differentiate into five layers: the Stratum Basale, the Stratum Spinosum, the Stratum Granulosum, the Stratum Lucidum, and the Stratum Corneum. The thickness of the epidermis is approximately 60-80  $\mu\text{m}$  but varies greatly with age, gender, and location on the body. For example, the epidermis on the underside of the forearm is few cell-layers thick, but is an order of magnitude thicker on the sole of the foot.

The dermis is the next major skin layer just below the epidermis. The dermis is approximately 1-2 mm thick in humans and is divided into two layers: the papillary dermis and the reticular dermis. The dermis includes collagen (Type I collagen) and reticulin (Type III collagen), which provide tensile strength. Elastic fibers provide for the restoration of shape after a deformation. Fibroblasts (synthesize collagen, elastin, and reticulin), histiocytes, endothelial cells, perivascular macrophages and dendritic cells, mast cells, smooth muscle, and cells of peripheral nerves and their end-organ receptors are the cell lines which are found in the dermis.

Below the dermis is the hypodermis (subcutis). This layer contains adipose tissue and serves to attach the dermis to its underlying tissues. This fatty tissue also serves as a heat-isolator, protective layer and energy reservoir. Larger blood and lymphatic vessels criss-cross this layer.



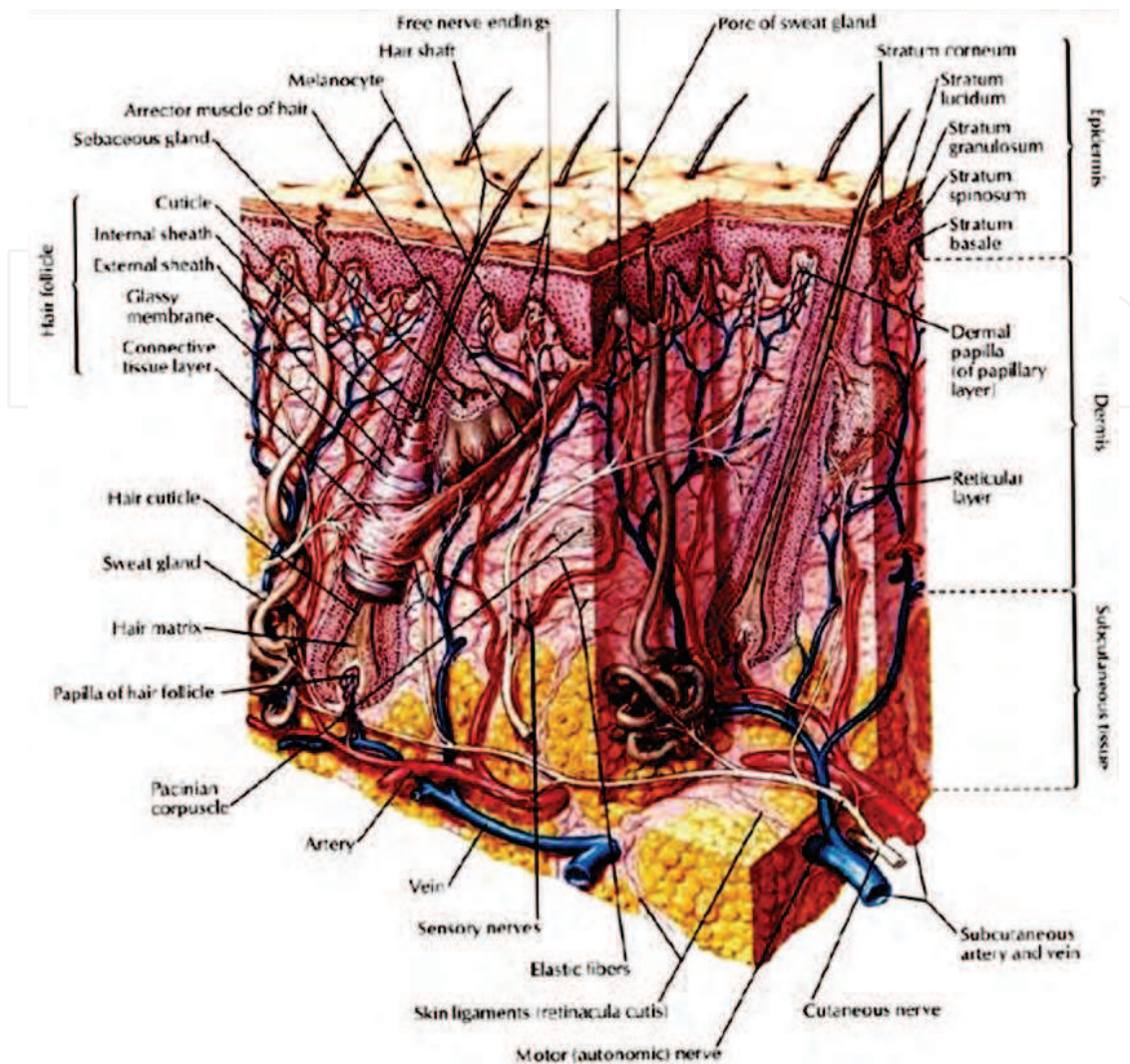


Fig. 1. Structure of the skin. Adapted from (Netter, 1997)

The skin is a highly inhomogeneous optical object and is almost impossible to mimic in a man-made phantom. Light interaction with the multilayer and multicomponent skin is a very complicated process. Non-uniform distribution of density and refractive index makes the skin a highly scattering media. Mean refractive index of background fluid can be calculated as weighted average of the refractive indices of interstitial fluid ( $n_{ISF}$ ) and cytoplasm ( $n_{cyt}$ ):

$$\bar{n}_{fluid} = \phi_{cyt} n_{cyt} + (1 - \phi_{cyt}) n_{ISF} , \quad (1)$$

where  $\phi_{cyt}$  is the volume fraction of cytoplasm in tissues and is approximately equal to 0.6. Average refractive indices of the interstitial fluid and cytoplasm are 1.355 and 1.367, respectively, yielding a refractive index for the background fluid of 1.362. The refractive index of other skin constituents such as melanin ( $n = 1.7$ ), collagen ( $n$  of fully hydrated = 1.43), adipose tissue ( $n = 1.46$ ), cellular nuclei ( $n = 1.39$ -1.41) and interstitial fluid ( $n = 1.34$ ) cause the dermis and the epidermis regions to be highly scattering in the NIR spectral region as the optical turbidity of tissues is mainly caused by the refractive index mismatch between the intracellular and the extracellular components.

The absorption coefficient  $\mu_a$  ( $\text{cm}^{-1}$ ) and the reduced scattering coefficient  $\mu'_s$  ( $\text{cm}^{-1}$ ) are two optical parameters used to describe the absorption and scattering properties of tissue. The absorption coefficient of skin expresses how far light of a particular wavelength can penetrate into the skin before it is absorbed. The reduced scattering coefficient is related to the scattering coefficient,  $\mu_s$  ( $\text{cm}^{-1}$ ), and the anisotropy factor of scattering,  $g$ , based on the relationship  $\mu'_s = \mu_s(1-g)$ ; it is used to describe the diffusion of photons in a random walk of step size of  $1/\mu'_s$ , where each step involves an isotropic scattering.

The penetration depth of light in skin is dependent on both the absorption and scattering coefficients, and also on wavelength. An estimation of the light penetration depth  $\delta$  can be performed with the relation:

$$\delta = \frac{1}{\sqrt{3\mu_a(\mu_a + \mu'_s)}} \quad (2)$$

In the ultraviolet (UV) and infrared (IR) ( $\lambda \geq 2 \mu\text{m}$ ) spectral regions, light is readily absorbed, which accounts for the small contribution of scattering and the inability of radiation to penetrate deep into skin (only through one or two cell layers) ; it is limited within the epidermis layer. For short-wave visible light, scattering and absorption both occur, with a penetration depth of 0.5 - 1.5 mm in human skin. In the wavelength range 0.6 - 1.4  $\mu\text{m}$ , the penetration depth in skin reaches 1.5 - 3.5 mm, and in this case, scattering prevails over absorption. When the wavelength is close to 2  $\mu\text{m}$ , the penetration depth appears relatively stable around 0.7 - 1.3 mm in skin.

### 3. Spoof detection using optical coherence tomography

In Section 2, we saw how the complexity of skin gives it optical properties that make it difficult to fake. In this section, we look at a new method of measuring those differences: optical coherence tomography (OCT). OCT allows us to see not only the surface of the skin but also some of the subsurface characteristics detailed in the last section. By extending the existing biometrics that are based on surface scan of external features, the OCT system can probe and extract the internal features of multilayered objects and tissues. The internal biometrics based technology is more robust against the tampering and counterfeiting comparing with conventional biometric systems.

Different approaches to OCT vary in both cost and effectiveness. We discuss OCT in general and the pros and cons of the various approaches. We then present the experimental results performed by Chang et al to demonstrate that OCT has great promise as a combine hardware and software approach to fingerprint analysis and liveness detection (Chang et al, 2006; Cheng et al, 2008).

#### 3.1 Internal biometrics

The traditional biometric technologies that are used for security and the identification of individuals primarily deal with fingerprints, hand geometry and face images. These traditional technologies use external features of the human body and can thus be easily spoofed or tampered with by distorting, modifying or counterfeiting the apparent features. The extraction of internal body features that are unique to individuals is now becoming a new trend for biometrics, which is termed "Internal Biometrics" (Chang et al, 2008).

In addition to the well-known technologies for iris and retina recognition, other versatile technologies for internal biometrics are currently being developed. Vein scan technology can

automatically identify a person based on the patterns of blood vessels in the back of the hand. Vein patterns are distinctive between twins, and even between a person's left and right hands. Developed before birth, they are highly stable and robust, changing throughout one's life only in overall size.

Skin pattern recognition technology measures the characteristic of an individual's skin. The exact composition of all the skin elements is distinctive to each person. For example, skin layers differ in thickness, the interfaces between the layers have different undulations, pigmentation differs, collagen fibers and other proteins differ in density, and the capillary beds have distinct densities and locations beneath the skin.

Iris recognition has been used as a biometric application since 1987. Iris recognition is based on the visible characteristics of the human iris, including rings, furrows, freckles, and the iris corona. Iridian's iris-recognition technology converts these visible characteristics into a template that can be stored for future verification. An 11-mm diameter iris can have 266 unique spots—compared to 10 to 60 unique spots for traditional biometric technologies. Another eye-related internal biometric feature involves retinal scanning, which analyses the layer of blood vessels at the back of the eye ([http://en.wikipedia.org/wiki/Retinal\\_scan](http://en.wikipedia.org/wiki/Retinal_scan)).

Fingernail-bed identification is based on the spatial distribution of the distinct grooves in the epidermal structure directly beneath the fingernail. This structure is mimicked in the ridges on the outer surface of the nail. When an interferometer is used to detect phase changes in back-scattered light shone on the fingernail, the distinct dimensions of the nail-bed can be reconstructed and a one-dimensional map can be generated.

Previous works have shown that the ear is a promising candidate for biometric identification. In a report (Yan and Bower, 2003), authors present a complete system for ear biometrics, including an automated segmentation of the ear in a profile view image and 3D-shape matching for recognition. Authors evaluated their system with the largest experimental study to date in ear biometrics, achieving a recognition rate of 97.6%. The algorithm they developed also shows good scalability of recognition rate with size of dataset size.

Fingerprints are the most commonly used type of biometric technology used for various applications, including law enforcement, financial transactions, access control, and information security. Fingerprint recognition has several benefits over other biometric identification techniques such as iris recognition, face recognition and hand-geometry verification methods. It has been revealed that fingerprint readers can be defeated either using cheap kitchen supplies, or by creating false thumbprint images. These attack methods are called "spoofing" because they attempt to fool a biometric system by presenting a fake fingerprint trait to the sensor. With less than \$10 worth of household supplies, artificial fingerprint gummies can be made and easily spoof the fingerprint system. Figure 2, 3 shows



Fig. 2. Dummy fingerprint made by polymer.





Fig. 3. Dummy fingerprint made by kitchen powder.

human fingerprints made by polymer, and by kitchen powder, respectively, on which all the visible external features are delicately created; these could successfully spoof a traditional fingerprint scanning system.

The following technologies have been proposed and tested both in hardware and software to defeat spoofing attacks:

1. Analyzing skin details through very high-resolution sensors (1000 dpi) to capture details such as sweat pores or coarseness of the skin texture.
2. Analyzing dynamic properties of the finger, such as pulse oximetry, blood pulsation, skin elasticity and skin perspiration.
3. Analyzing static properties of the finger by adding hardware to capture information such as temperature, impedance or other electric measurements, and spectroscopy.
4. Using multi-spectral imaging technology to measure the fingerprint characteristics that are at and beneath the surface of the skin.

To detect and explore the internal features for internal biometrics, special tools which have the capability of penetrating the bio-sample are needed. Having features of  $\mu\text{m}$ -level resolution of cross-sectional image, non-contact probing, and relatively cheap cost, optical coherence tomography becomes the best candidate for internal biometric applications.

### 3.2 Principles of OCT

Optical coherence tomography is an emerging technology for high-resolution cross-sectional imaging of 3D structures. The first OCT system was reported by Huang et al in 1991. Since then, OCT technology has been attracting the attention of researchers throughout the world. OCT relies on the interferometric measurement of coherent backscattering variations to detect internal interface structures of tested samples, such as biomedical tissues or internal scattered and layered materials. While similar to ultrasound B-mode imaging, OCT uses an infrared light source rather than ultrasound.

OCT has several advantages over other volume-sensing systems:

- Higher resolution: This feature enables greater visualization of details. Normally OCT has a cross-sectional resolution about 5-20 microns. For comparison, ultrasound has a resolution of 150 microns; high-resolution CT has 300 microns; and MRI has 1,000 microns.
- Non-invasive, non-contact measurement: This feature increases safety and ease of use and extends the possibility for *in vivo* applications, which is important for biological applications such as biometrics.



- Fiber-optics delivery: As optical fiber diameter is normally 125 microns, it allows OCT with a miniature optic fiber probe to be used for in situ applications, particularly for tiny lumen and intravascular applications.
- High speed: The new generation of OCT technology has no mechanical scanning procedures. This allows for high-resolution 3D sensing by the full-field OCT system.
- Potential for obtaining additional information from the testing sample: Many optical properties of samples could be explored by functional OCT. For examples, polarization contrast, Doppler Effect, and spectroscopic information.
- Use of non-harmful radiation. OCT systems work with visual and infrared band, unlike traditional CT working with X-ray and ultrasound relying on mechanical vibration.

In the past decade, OCT systems have been developed mainly for medical and biomedical applications, especially for the diagnostics of ophthalmology, dermatology, dentistry (Smolka, 2008) and cardiology. To explore the capabilities of OCT system for probing the internal features of an object, references (Chang et al, 2006) reported the applications for multiple-layer information retrieval and internal biometrics (Cheng and Larin, 2006; Chang et al, 2008). In addition, because OCT has the voxel resolution of micrometer size, it has potential applications in material investigation (Wiesauera et al, 2005; Bashkansky et al, 2001; Chinn & Swanson, 1996; Dunkers et al, 1999) and artwork diagnostics. Reference (Targowski et al, 2006) describes OCT diagnostics used for museum objects, involving stratigraphic applications (Szkulmowskaki et al, 2007); varnish layer analysis (Liang et al, 2005; Rie, 1987); structural analysis and profilometric applications (Spring et al, 2008; Targowski et al, 2004 ; Yang et al, 2004; Targowski et al, 2006). In Reference (Szkulmowska et al, 2005), the use of different OCT systems for oil painting layer examination, varnish thickness determination, and environmental influence on paintings on canvas are described. To explore the capabilities of OCT systems for probing the internal features of an object, authors have performed research in applying OCT technology for information encoding and retrieving with a multiple-layer information carrier. Since OCT has a resolution on the scale of microns and is able to peel cross-sectional images from the inside of an object, it has potential applications in documents security and object identification.

In direct imaging using an ordinary camera, all of the layers reflected from the surface of an object will be fused together in the resulting image. However, in optical coherence tomography imaging, a coherence gate generated by an interferometer and broadband light source could be used to extract cross-sectional images at different depths. The depth resolution of an OCT system is determined by the bandwidth of the light source, normally, the bandwidth is around 100 nm, and the depth resolution in air is about 7  $\mu\text{m}$ .

### 3.2.1 Time-domain OCT

OCT technology originates from low coherence interferometry (LCI) (a nonscanning /imaging version of OCT) where axial (depth) ranging is provided by linearly scanned low-coherence interferometry. This method of signal acquisition is referred to as time-domain OCT (TD-OCT). TD-OCT system is typically based on a Michelson interferometer. There are two main configurations: free space and fiber-based setups.

In TD-OCT systems, a broadband light source is used in a Michelson-type interferometer. A mechanical scanning device is introduced to select different layers at different depths by moving a reference mirror (Figure 4 shows the basic concept). With a broadband light source, the motion of the mirror produces moving interference fringes, called a coherence

gate, which scan through the sample. For imaging with an ordinary camera, all of the reflected/scattered light from different layers,  $L_1, L_2 \dots L_n$ , are collected together and form a fused image. However, in OCT imaging, only the layer whose optical length is the same as that in the reference arm gets modulated by the interfering fringes, i.e., framed by the coherence gate. Using a specially designed algorithm, the image of this layer can be extracted from the others. Sources with broader bandwidths have a narrower gate, and achieved finer resolutions in the cross-sectional images that are extracted.

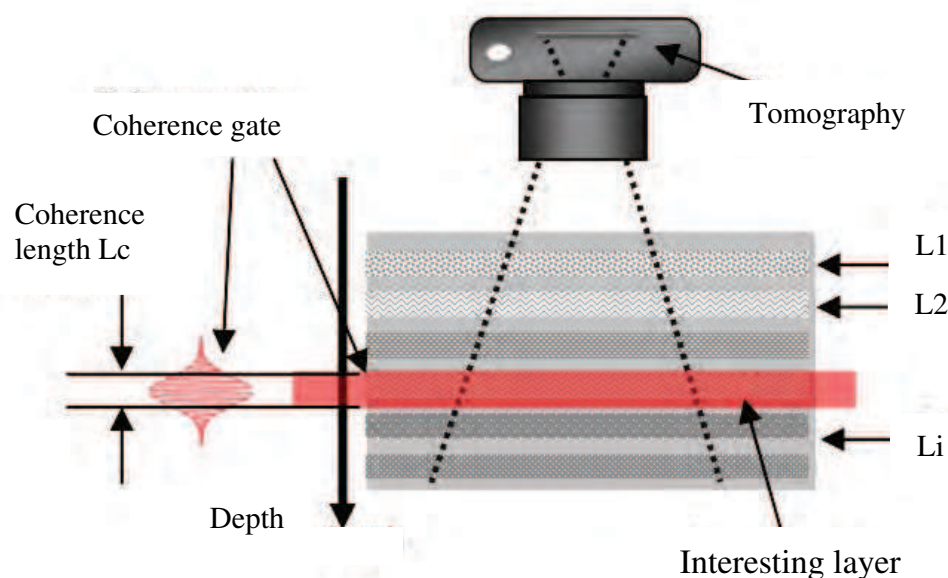


Fig. 4. Coherence gate used for separating layers

### 3.2.2 Full-field OCT

Most OCT systems are fiber-optic interferometers, a technology based on point-scanning. To get an enface image, i.e., an image consists of many A-scans, the 2D scanning is a must. Depth scanning is achieved by the longitudinal translation of a reference mirror for TD-OCT. Such a 3-axis scanning procedure makes the system slow and cumbersome. Parallel detection schemes have been investigated to increase the acquisition speed and eliminate the need for lateral scanning. Parallel OCT systems illuminate the entire 2D target and collect light from all pixels simultaneously. These parallel OCT systems are often called full-field OCT systems (FF-OCT) (Dubois et al, 2002; Akiba et al, 2007). A few OCT systems working directly on 2D full-field images have been reported. Figure 5 shows a FF-OCT system using two cameras that can perform real-time video-rate OCT imaging.

For a typical OCT light source, a super-luminescent laser diode (SLD) with central wavelength 830nm and 15 nm bandwidth, the system resolution has a depth resolution of 20  $\mu\text{m}$ . To further increase the resolution of an OCT system, the broadband light source is needed. A very good candidate for the broadband light source is a white light source such as a halogen lamp. The combination of white light interferometric techniques with modern electronics and software can yield powerful measurement tools. White-light interferometry methods have already been established for the measurement of topographical features of sample surfaces, and these can be further modified to extract the cross-sectional image of an object (Chang et al, 2008). In the presented white light TD-OCT system, we use a halogen light source with a central wavelength of 700 nm and bandwidth of 200 nm. The depth resolution is 0.9  $\mu\text{m}$ . The image grabbing rate can achieve 30 frames/second, with a

resolution of 1024x1024 pixels at 12-bit gray levels. The mechanical depth scanning accuracy is 37 nm. For such a high-accuracy system, alignment and fine-tuning is critical. A technology, combining automatic vision and motion control, was developed to perform this task. The imaging area is designed for 25 mm by 25 mm, which is good for most of the fingerprints. As the halogen lamp has very high power, the working area can be extended even larger. This system was built for fingerprint and document security, as well as 3D sensing.

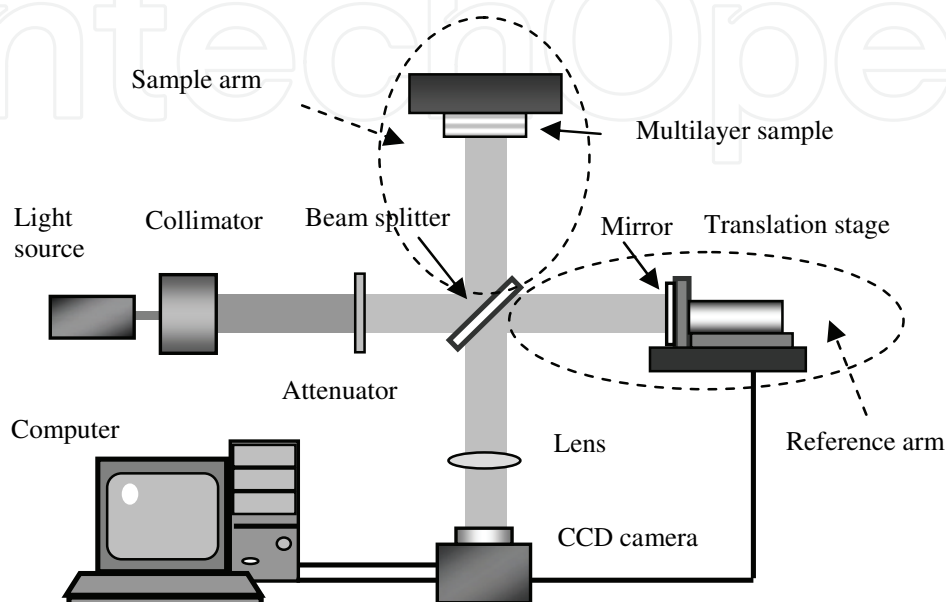


Fig. 5. FF-OCT system

### 3.3 Dummy fingerprint detection using OCT systems

#### 3.3.1 Detection performed by fiber-based OCT system

##### 3.3.1.1 Description of TD-OCT system and preparation of artificial fingerprints

TD-OCT systems are useful for the noninvasive identification of artificial materials that can be used to bypass fingerprint biometric devices. High in-depth and lateral resolution versions of this technique, along with real-time image acquisition, allow for the identification of false fingerprints by analyzing the sample's optical properties to detect any extra layers of artificial materials placed on a finger.

Figure 6 shows a diagram of a TD-OCT system used in these studies. A low-coherence SLD with a wavelength of  $1300 \pm 15$  nm and an output power of 10 mW was used as the optical source in this system. Light in the sample arm of the interferometer was directed into the tissue sample using a single-mode optical fiber and an endoscopic probe.

The endoscopic probe allowed for the lateral scanning of sample surfaces. Light scattered from the sample and light reflected from the reference arm mirror form an interferogram that is detected by a photodetector. In-depth scanning was produced electronically by piezoelectric modulation of the fiber length, and 2D images were obtained by scanning over the sample surface in both the lateral direction (X-axis) and in-depth (Z-axis). Operation of the TD-OCT system was fully computer-controlled. The resulting images were 450 by 450 pixels with a full-image acquisition rate of approximately 3 seconds. In-depth scanning was up to 2.2 mm (in air), while lateral scanning was over 2.4 mm. Figure 7(a) shows typical

OCT image of the skin of a finger. Three layers of human skin (the stratum corneum, epidermis and dermis) are clearly visible. The 2D images were then averaged in the lateral dimension over  $\approx 1$  mm (sufficient for speckle-noise suppression) to obtain a single curve. The output OCT signal represents the 1D distribution of light in depth (plotted on a logarithmic scale), as shown in Figure 7(b). The resolution obtained by the system was estimated at about  $25\text{ }\mu\text{m}$  in air, corresponding to about  $19\text{ }\mu\text{m}$  in tissues (assuming refractive index of 1.4).

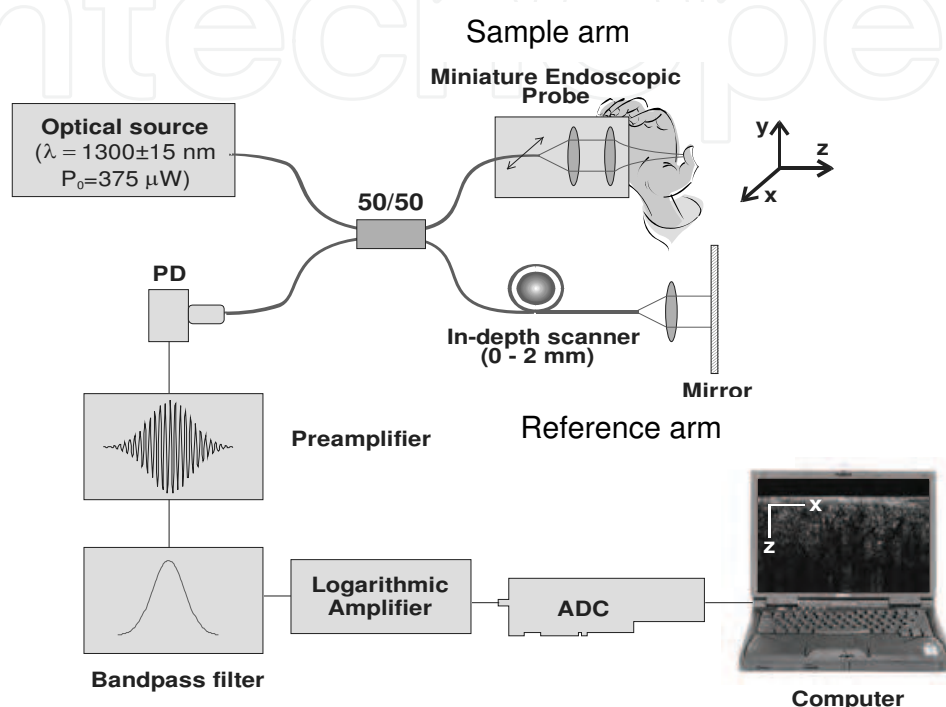


Fig. 6. Schematic diagram of the TD-OCT system (PD = photo detector, ADC = analog-to-digital converter).

This fiber-based TD-OCT system was used to study different artificial materials that might be used in preparation of artificial fingerprints. Artificial fingerprint dummies were made using a plasticine (Dixon Ticonderoga Company, Mexico), a household cement (ITW Devcon Corporation, MA), and a liquid silicone rubber (GE Silicones, General Electric Company, New York). We used general household materials that could be found in any supermarket. The following procedures were followed to make an artificial fingerprint dummy (male mold) from the plasticine (female mold).

The plasticine was cut and kneaded into thick pieces for the preparation of a female mold. To obtain the best imprint of the original fingerprint patterns, the finger was carefully washed with soap to get rid of any dust and oil. The finger was then pressed firmly into the plasticine to leave a fingerprint pattern (female mold, Figure 8(a)). To prepare the male mold, we poured glue or liquid silicone rubber into the female mold. After natural solidification, the dummy was removed and its fingerprint surface was carefully wiped to remove plasticine pieces (internal impurities such as air bubbles or tiny pieces of plasticine were still present, although the OCT images were obtained from regions that were free from structural defects). At this point, the artificial fingerprint dummy (male mold) was ready for experimentations (as shown in Figure 8(b)).



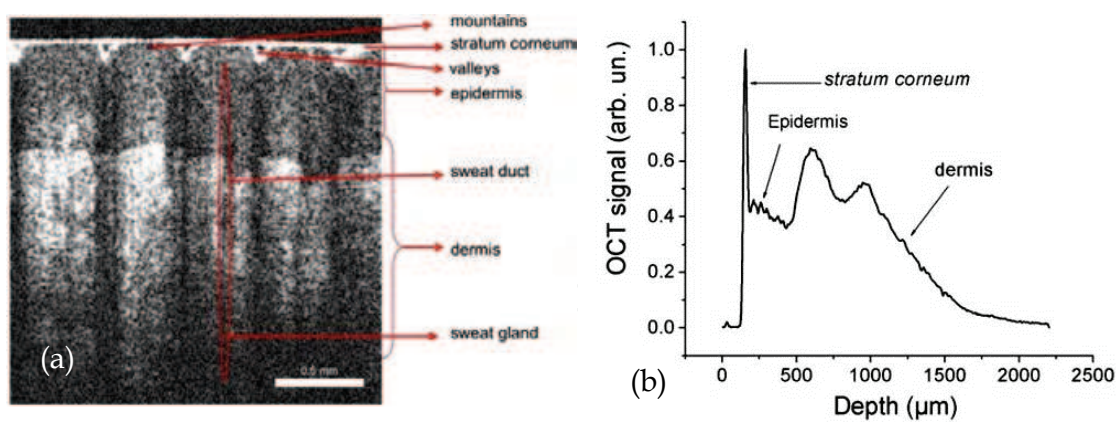


Fig. 7. A typical OCT image obtained from the skin of a thumb (a) and the corresponding OCT signal (b) showing the depths of the major skin layers.

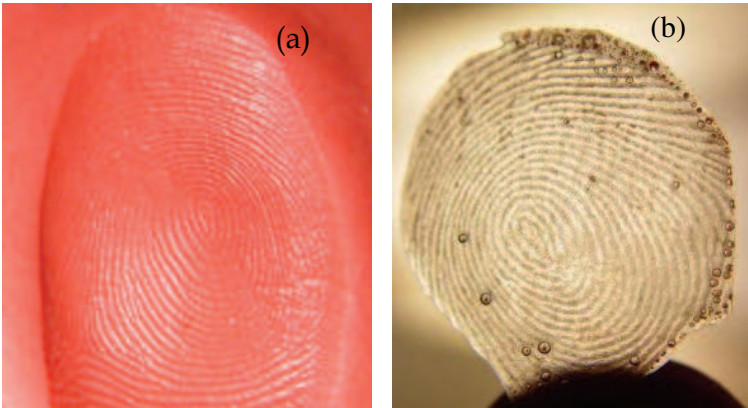


Fig. 8. Dummy fingerprint (a) Plasticine fingerprint (female mold) (b) Artificial fingerprint dummy (male mold)

The plasticine was cut and kneaded into thick pieces for the preparation of a female mold. To obtain the best imprint of the original fingerprint patterns, the finger was carefully washed with soap to get rid of any dust and oil. The finger was then pressed firmly into the plasticine to leave a fingerprint pattern (female mold, Figure 8(a)). To prepare the male mold, we poured glue or liquid silicone rubber into the female mold. After natural solidification, the dummy was removed and its fingerprint surface was carefully wiped to remove plasticine pieces (internal impurities such as air bubbles or tiny pieces of plasticine were still present, although the OCT images were obtained from regions that were free from structural defects). At this point, the artificial fingerprint dummy (male mold) was ready for experimentations (as shown in Figure 8(b)).

3.3.1.2 In-depth analysis of structural characteristics of TD-OCT images

Several materials that can be used to make artificial fingerprints have been studied, including gelatin, silicon, wax, and agar. Figure 9 illustrates an OCT image and the corresponding signal curve typical of a gelatin layer (25% concentration) placed over a finger. The artificial gelatin layer and the human skin layers beneath it can be clearly detected in both Figures 9(a) and 9(b). The gelatin layer is a homogeneous medium and has a significantly lower scattering profile than that of the skin, as illustrated by the OCT signal

curve between 0 and 0.2 mm. The characteristic layers of the human skin under the gelatin layer can be identified as in Figure 7(b).

Typical results obtained from a 0.2 mm thick layer of 10%-concentration agar over a thumb are shown on Figure 10. The resulting OCT image is shown in Figure 10(a), and the corresponding signal in Figure 10(b) shows the thickness of the agar and its scattering profile. Similarly, Figure 11(a) shows the OCT image of a thumb with an outer layer of silicone of 0.08 mm average thickness. The corresponding 1D graph in Figure 11(b) shows that the layer of silicon is easily distinguishable. Finally, an OCT image and the corresponding signal for a wax sample placed on a thumb are shown on Figures 12(a) and 12(b), respectively.

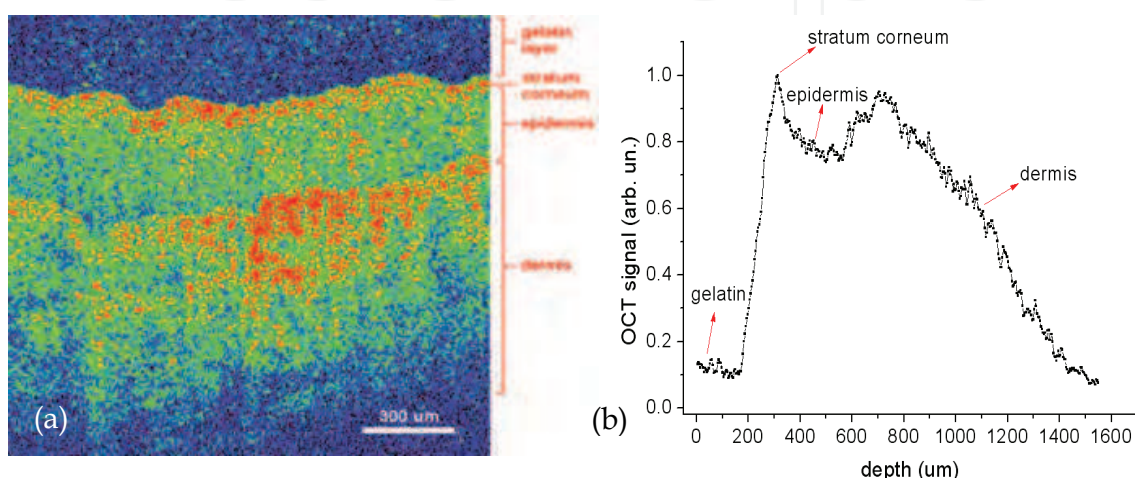


Fig. 9. OCT image (a) and the corresponding signal (b) of 25%-concentration gelatin placed over skin.

Typical results obtained from a 0.2 mm thick layer of 10%-concentration agar over a thumb are shown on Figure 10. The resulting OCT image is shown in Figure 10(a), and the corresponding signal in Figure 10(b) shows the thickness of the agar and its scattering profile. Similarly, Figure 11(a) shows the OCT image of a thumb with an outer layer of silicone of 0.08 mm average thickness. The corresponding 1D graph in Figure 11(b) shows that the layer of silicon is easily distinguishable. Finally, an OCT image and the corresponding signal for a wax sample placed on a thumb are shown on Figures 12(a) and 12(b), respectively.

To demonstrate the usefulness of OCT as a detection technique, a commercially available fingerprint reader device (Microsoft Fingerprint Reader, Model: 1033, Redmond, WA) was tested in some experiments. The fingerprint patterns of a volunteer's thumbs, forefingers, middle fingers and ring fingers from both the left and right hands were recorded and registered on a computer. The same fingers were used to prepare the artificial dummies. The dummies were then placed on another person's fingers and were scanned using both the fingerprint reader and the OCT system. Each dummy was tested 10-20 times using both systems and the corresponding FARs (False Accept Rates) were calculated. FAR represents the likelihood that the biometric security system will incorrectly accept an access attempt by an unauthorized user. When these artificial dummies were applied to the reader, the resulting FARs were from 80% to 100%. However, the artificial fingerprint dummies were always detected by the OCT system and the FARs were reduced to 0%.

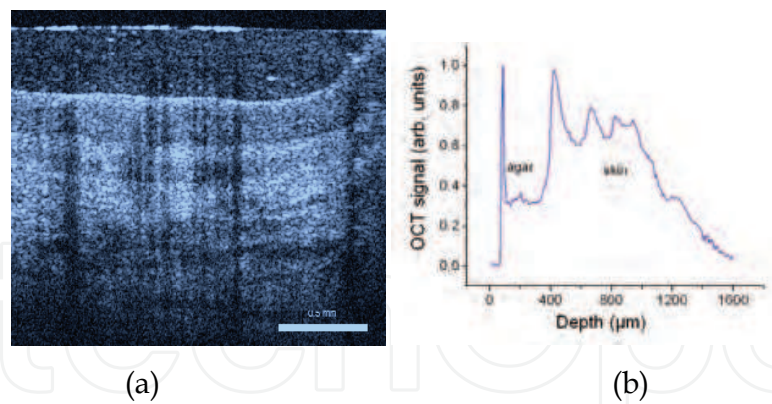


Fig. 10. OCT image (a) and corresponding OCT signal (b) obtained from 10% agar of average thickness of 0.2 mm over a thumb.

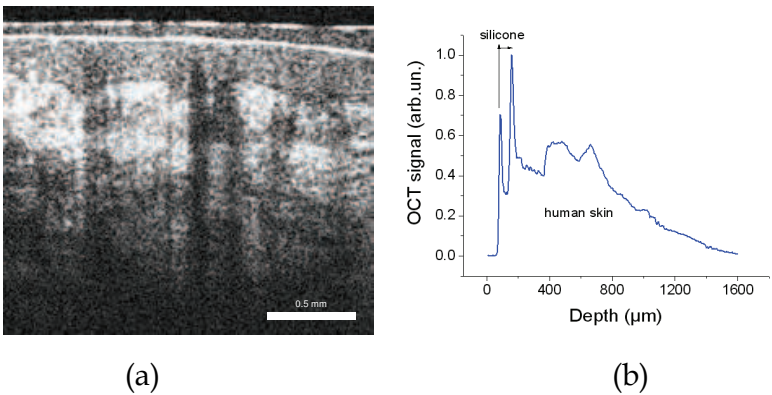


Fig. 11. OCT image (a) and corresponding OCT signal (b) obtained from silicon of average thickness of 0.08 mm over a thumb.

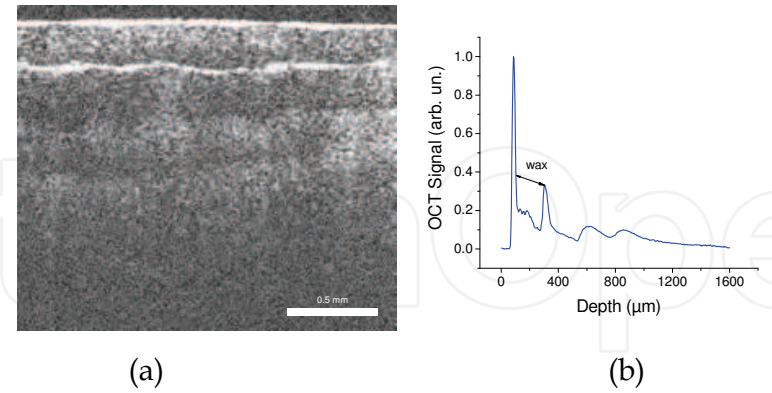


Fig. 12. OCT image (a) and corresponding OCT signal (b) obtained from wax over a thumb.

3.3.1.3 In-depth analysis of tissues optical properties

Another method for identifying artificial materials is based on an analysis of their optical properties. Previously, we and others demonstrated that by analyzing the exponential profile of light distribution in tissues, one can calculate its scattering coefficient. Similarly, an analysis of the optical properties of several artificial materials relative to that of human skin has revealed that it can be used for differentiation purposes. The OCT signals were



plotted on a logarithmic scale and the slopes of the OCT signal (OCTSS) were calculated at regions corresponding to artificial materials and human skin using a least-squares algorithm. Table 1 shows the calculated OCTSS values for the materials studied. From this table one can see that OCTSS (and, thus, the optical properties) of all studied artificial materials are significantly different from that of skin (except for samples made of wax). These results demonstrate that this method may help in identifying artificial materials present on human skin.

Results shown in Table 1 also demonstrate that the fingerprint dummies prepared using wax could have similar optical properties as for the dermis. Therefore, it might be difficult to differentiate wax-based artificial materials from the skin based solely on calculation of its optical properties. In such cases, combination of two or more methods might be required for more robust identification of artificial materials placed on real skin.

Concentration / OCTSS	Gelatin	Agar	Skin (dermis)	Wax	Silicone
100%			1.0	1.25	0.08
10%	0.07	0.15			
25%	0.18	0.33			
33%	0.20	0.38			

Table 1. OCT signal slopes calculated for the different materials (gelatin, agar, silicone, and wax) relative to that of human dermis.

3.3.1.4 Autocorrelation analysis of speckle variance in OCT images

Another method for robust identification of fingerprint dummies is based on a multidimensional autocorrelation analysis of OCT images. Autocorrelation refers to the cross-correlation of a signal with itself, and is a commonly used method in signal processing to analyze functions and series. Autocorrelation analysis is a useful technique in the search for repeating patterns, such as periodic signals that have been buried in noise, e.g. speckle noise. Speckles result from the coherent superposition (mutual interference) of light scattered from random scattering centers. In OCT imaging of scattering media, the speckle noise results from the coherent nature of laser radiation and the interferometric detection of the scattered light. Speckle noise substantially deteriorates resolution and accuracy of the OCT images and, therefore, several methods have been proposed to reduce its effect. However, speckle noise bears useful information about an object’s properties and can be utilized in tissue classification and monitoring of different processes.

Recently, we obtained encouraging results in the application of autocorrelation analysis for distinguishing gelatin- and agar-based fingerprint dummies from skin. The method is described as follows. Two-dimensional OCT images are converted into relative intensity values and these are recorded in a square matrix (450×450 pixels). Each column in the matrix contains information about one independent Z-scan of the OCT system. A discrete autocorrelation method is applied to process data in all columns. We define the function  $u(d)$ , for a column intensity data in the image matrix, where  $d$  is the depth ranging from 1 to 450 pixels (corresponding depths of to 0 - 1.6 mm in the sample with a refractive index of



1.4). Before autocorrelating, we remove the mean value of  $u(d)$ , as  $x(d)=u(d) - \mu$ , where  $\mu = \frac{1}{N} \sum_{n=1}^N u(d)$  was the mean value of the function  $u(d)$ . The discrete autocorrelation function for  $x(d)$  is

$$R_{xx}(r\Delta d) = \frac{1}{N-r} \sum_{n=1}^{N-r} x_n x_{n+1} = \frac{1}{N-r} \sum_{n=1}^{N-r} x(d) x(d+r\Delta d) \quad (10)$$

in which  $r$  is the depth number such that  $r=0,1,2,\dots,m$  ( $m < N$ ),  $m$  refers to the maximum depth of autocorrelation,  $\Delta d=1$  - space interval unit (with value of 1 OCT pixel),  $N$  is the total available depth for a given region of an OCT signal curve used in the autocorrelation analysis (either the artificial material or real skin). The value of  $N$  differs for the autocorrelation functions in the artificial material and the human real finger regions; we use  $m = N-1$ , where  $m=50$  for the artificial material region (the artificial fingerprint), and  $m=100$  for the real finger region. Using this algorithm, we calculate the autocorrelation function in each column of the OCT signal matrix and then average to find the arithmetic mean value.

Figure 13 shows encouraging results obtained from the autocorrelation analysis of gelatin, agar, and real finger samples. The autocorrelation analysis was applied in the regions of OCT images corresponding to the artificial materials and human skin. Depth, shown in pixels (1 pixel is approximately equal to  $3.5 \mu\text{m}$ ), refers to the interval where the OCT signal compared with itself. As depth increases, the autocorrelation function values for gelatin and agar fall sharply to zero due to the homogeneous structure of the artificial materials. Since

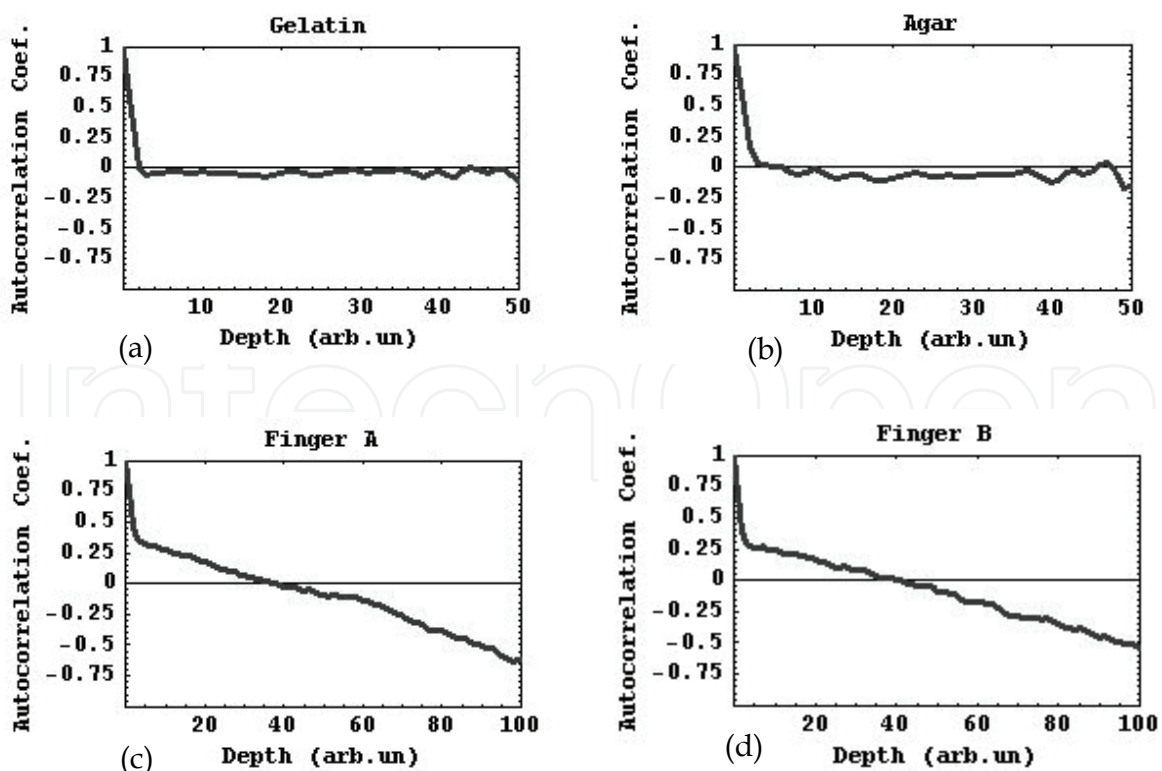


Fig. 13. Autocorrelation curves for artificial materials: (a) gelatin, (b) agar, (c, d) human fingers.

the fluctuations of the speckle intensity in the OCT images are random and homogeneous in these regions, the autocorrelation function values at each depth are around zero. Unlike the artificial material, human skin is a highly inhomogeneous tissue. When the autocorrelation analysis is applied to skin, the resulting autocorrelation function curves (Figures 13 (c) and (d)) decrease nearly monotonically with increasing depth and therefore differ significantly from the artificial materials. As a result, an autocorrelation analysis of OCT speckle-noise could potentially be used as a criterion for automatic and semi-automatic discrimination of artificial materials from real fingers.

### 3.3.2 Detection using full-field OCT systems

In section 3.2.2, the full-field OCT, FF-OCT, has been introduced. Because it has the capability of grabbing A-scans in parallel, FF-OCT system has much higher processing speed. In this sub session, we will describe detection of dummy fingerprint using FF-OCT systems.

As dummy fingerprints are normally made using translucent materials, the full-field OCT becomes a powerful tool for quickly and effectively distinguishing real fingers from artificial ones. FF-OCT can detect both surfaces of a dummy – the fingerprint surface as well as the non-print surface – and can probe the internal structures within them. The features observed using an FF-OCT system will differ from those for a real finger, as demonstrated in the set of cross-sectional images shown in Figure 14. Two obvious surfaces exhibiting different features were discovered during the depth scanning. The outer surface shows a smooth 2D curve (Figures 14(a)–14(f)), a feature that does not exist in a real fingerprint. However, the inner surface shows segmented fingerprints at different layers (Figures 14(g)–14(l)).

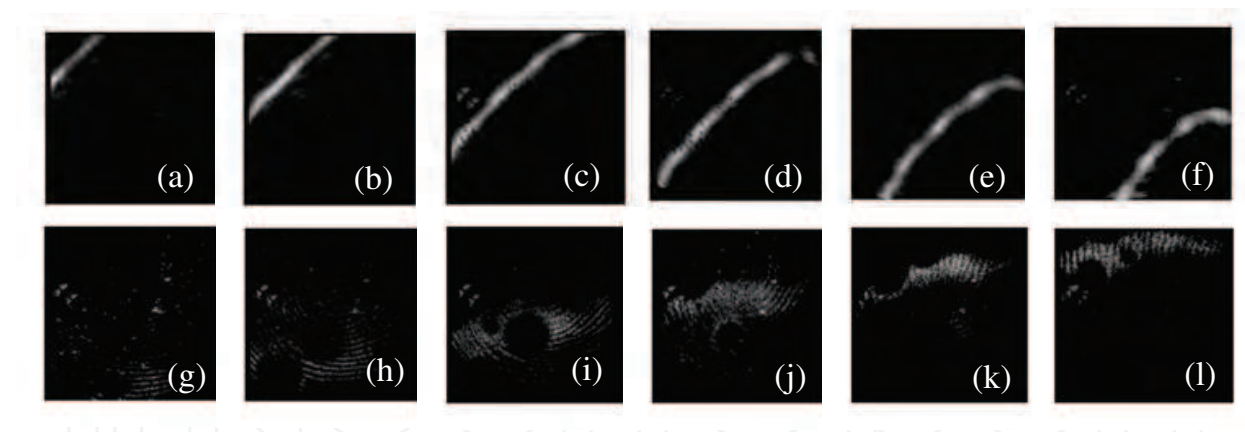


Fig. 14. OCT Images of a dummy fingerprint obtained by a FF-OCT system (a)–(f). OCT images extracted from the outer surfaces (layer distance: 50  $\mu\text{m}$ ). (g)–(l). OCT images extracted from the inner surfaces (layer distance: 20  $\mu\text{m}$ ).

The summation of Figures 14(a)–14(f) is shown in Figure 15(a), which reveals a bright area without any fingerprints in it. (The image sampling separation is set to 50  $\mu\text{m}$ , so that the black fringes appear when these two images are overlapped). Figure 15(b) shows the summation of the segmented fingerprints from Figures 14(g)–14(l). Figure 15(c) gives the summation of all the tomographic images, wherein which the fingerprint image is completely destroyed. The summation is very different from the image captured by a common 2D camera used in a fingerprint recognition system, as shown in Figure 15(d).

Figure 16 provides another set of rotated 3D volume data. The red parts show the internal structure of the dummy, which is totally different from the internal tissues in a real finger. The presence of the two surfaces and their distinct patterns reveal that the scanned object is a fingerprint dummy.

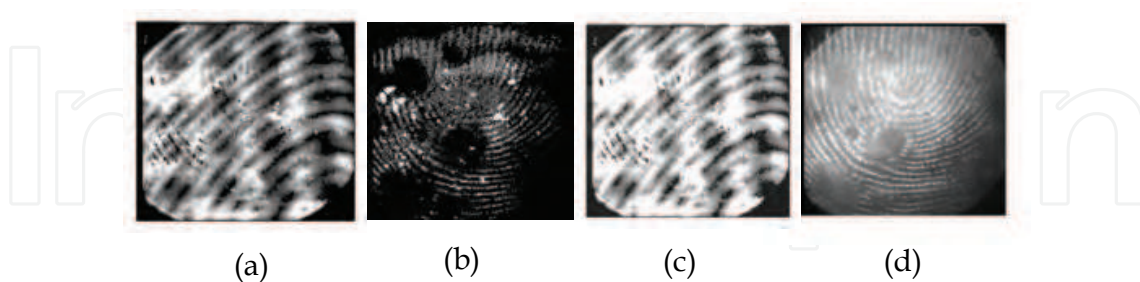


Fig. 15. Images of a dummy fingerprint. (a) OCT image of the outer surface of dummy. (b) OCT image of the inner surface of dummy. (c) Summation of above images (a) and (b). (d) Direct imaging of the dummy by a camera

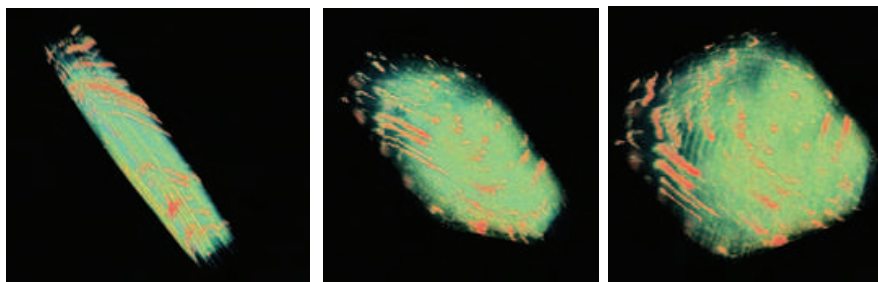


Fig. 16. Three rotated images of the 3D volume data of a dummy fingerprint.

In a traditional fingerprint reader, the finger must be pressed on a transparent flat surface in order to produce a 2D fingerprint pattern. There are some problems associated with these types of devices. Firstly, any motion of the finger may blur the imprinted image. Secondly, obtaining a clear image requires that the imprinting surface be cleaned for every new user, which adds complexity to the mechanical implementation. Another important issue lies in the fact that the 2D (flat) fingerprint pattern loses 3D-profile features that also provides information that can be used to uniquely identify an individual. The OCT-based fingerprint recognition system integrates all of the 2D morphologic features, along with the 3D profile and internal structure, which increases the ability of the system to robustly discriminate artificial fingerprints from real ones.

#### 4. Spoof detection using spectral analysis

As previously described, fingerprint readers can be defeated using artificial (or prosthetic) fingers that can be created from cheap kitchen supplies or polymeric materials. These methods are commonly called “spoofing” because they are attempts to spoof the credentials of a valid user by presenting a fake fingerprint trait to the biometric sensor. Fingerprint spoofing uses simple techniques that can be quite effective (see Figure 17), so spoof detection is becoming increasingly important.

To address the threat of spoofing, we investigate the possibility of detecting artificial fingers by using spectrum analysis. In this section, we will first study the characteristics exhibited when human and fake fingers are exposed to different wavelengths of light. Based on the spectral images, we develop an algorithm to process the captured image, calculate the average image energy, extract the spectral features, and then distinguish the artificial fingers from the real ones.



Fig. 17. Steps to make a dummy finger using a cheap kitchen powder

4.1 Differences between real finger and fake finger

A living human finger has rich blood vessels, sweat glands, and soft tissues under the skin. A cross-sectional image of a real finger extracted by an OCT system is shown in Figure 18. This image shows that the underlying morphology has layered tissues with some sweat glands. This complicated structure causes a strong scattering when light is shone on the surface. Because human tissue mostly consists of water, the absorption of the incident light is quite strong and varies according to the wavelength applied.

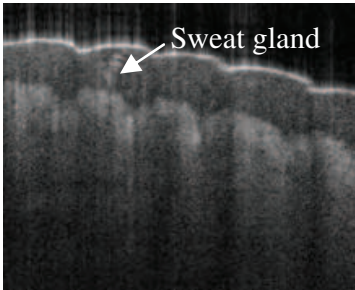


Fig. 18. OCT image of a real finger

The dummy or prosthetic finger is made by casting a real human finger with silicon or polymer material, and then painting the skin color, hair, even a nail on its surface. (Figure 19).



Fig. 19. The real finger (bottom) and the prosthetic finger (top) made from it.



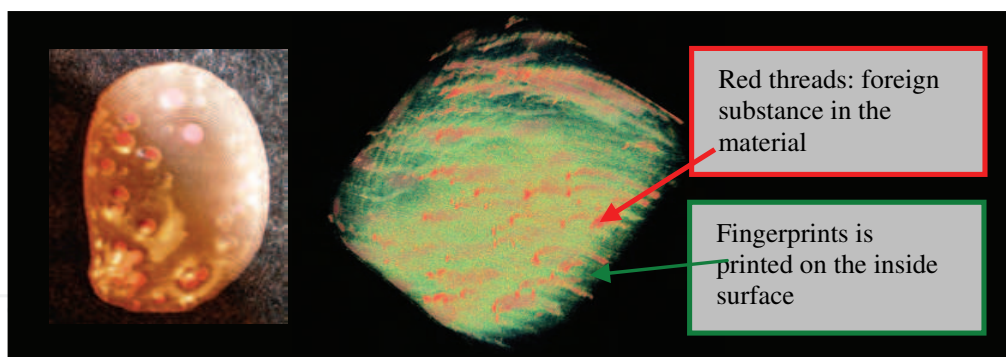


Fig. 20. A dummy fingerprint and its 3D OCT volume structure

Since no internal bio-structure information exists within the prosthetic finger, there must be a significant difference in the optical properties between it and a real finger. Figure 20 illustrates the 3D volume structure (right) of a dummy fingerprint casting from a person (left). This 3D volume data was obtained by the FF-OCT system described in the previous section. None of the red threads inside the volume exist in the real human finger. Comparing to the layered structure shown in Figure 18, the optical properties of the reflected light from dummy finger should be quite different.

#### 4.2 Finger image spectrum analysis

A fingerprint imaging system was constructed to explore the spectral features of the real and fake fingers, and is shown schematically in Figure 21. The imaging system has the following specifications:

- Light source: Broadband white light with a mercury arc lamp. An attenuator is used to change the intensity of the light.
- Filters: Nine wavelength filters from near ultraviolet through visible light to near infrared (400nm, 450nm, 500nm, 550nm, 600nm, 650nm, 700nm, 800nm, 850nm).
- Camera: Dalsa 1M15 CCD, which covers the visual band (with the original lens) and the near infrared band (with the original lens removed).
- Imaging: To avoid the sensitivity to oil or dirt contaminates, there was no glass used in front of the finger during the fingerprint acquisition.
- A computer was used for image acquisition and processing.

Each test's finger was placed on the finger holder, and nine images were grabbed for each person or sample. The output intensity of the light source, and the attenuator in front of the camera, was adjusted in order to get the best image quality. Six human fingers and one prosthetic were tested in this project. They are three Asian adults (two male and one female); two white adults (one male and one female); one black adult male; and one prosthetic finger (shown in Figure 22) reproduced from one of the Asian male subjects.

The procedures involved in the spectrum analysis are illustrated in the flowchart of Figure 23. The input is a 1024x1024 pixel image with 16-bit grey scale. A nonlinear median filter is used to preserve edges while removing noise. A normalization process is carried out to reduce the effects of differences in illumination, skin reflection and ambient light. All the values are normalized between 0 and 255. A banded image is created to collect the energy reflected from the central area of the finger (Figure 24). In the experiments, band parameters are X direction 300 pixels and Y direction 300 pixels centered in the image. Average energy (AE) is calculated by averaging the pixel values over the banded image area. The Canny

edge detection algorithm is implemented to detect the edges with a scaling factor of 25%. The detected edges are used to generate a mask. Edge energy (EE) is measured by averaging the image values under the mask. A decision function is constructed based-on the average of image energies AE and EE. The output status is “true” if the input is detected as a real finger and “false” otherwise.

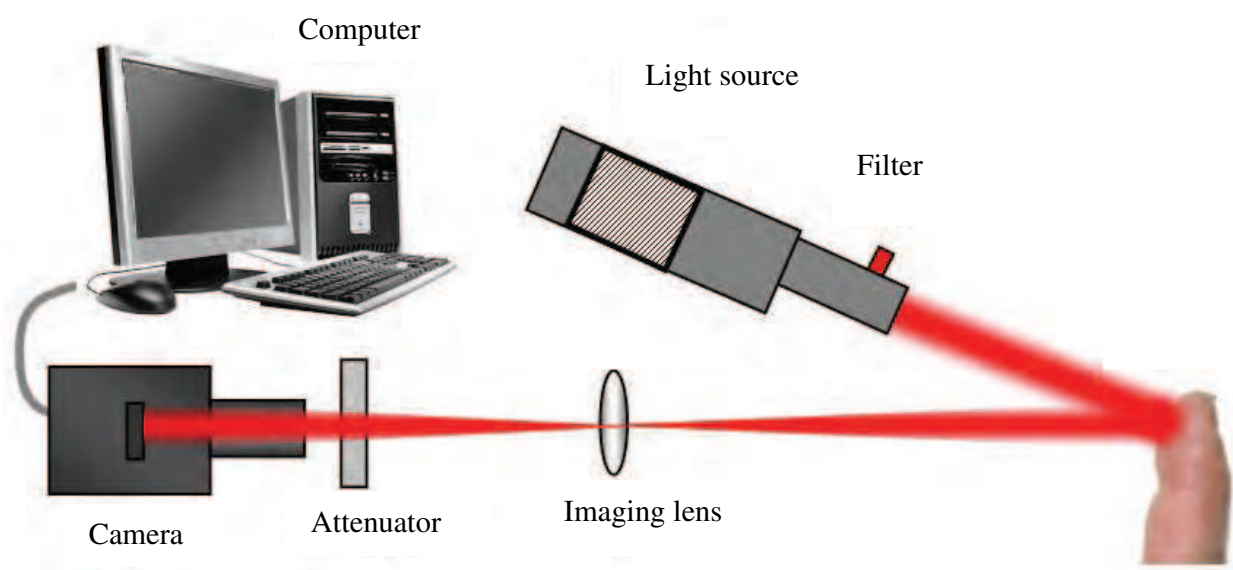


Fig. 21. Fingerprint imaging system configuration.



Fig. 22. Fake finger used in experiments.

Figure 25 shows finger images and the corresponding edge images for a real finger and its equivalent artificial finger. From those edge images, we observed that: 1) At short wavelengths, particularly at 400 nm (near ultraviolet), both the real and artificial fingers show more edge details than those extracted using longer wavelengths. 2) At longer wavelengths, particularly at 850 nm (near infrared), the artificial finger image becomes blurred. Nevertheless, we observe that the artificial finger is much brighter at longer wavelengths, especially at 850nm, even though the images were taken under the same conditions and were normalized using the same algorithm.

These observations can be explained by differences in the optical properties between human skin and materials, normally polymers, used in the fabricated artificial fingers. The *in vivo*

absorption coefficient of human skin is about 70% of the absorption coefficient of water, and the isotropic scattering coefficient ranges from 3 to 16  $\text{cm}^{-1}$ , much stronger than that of polymers. Because human tissue absorbs more light than polymers at wavelength greater than 700 nm, there is more back-reflected and scattered light collected by the camera for the artificial finger; this means that the artificial finger image contains more energy, or optical power. At the same time, since the back-reflecting and scattering light from the deeper penetration lacks the additional structural information found in human skin, it overwhelms the ridge information reflected from the surface. This lack of internal structure is the reason why the fake finger images appear more blurred. The blurring effect is measured by the average energy of the edge image of a finger: the fewer edges detected in an edge image, the lower the average edge energy the image contains.

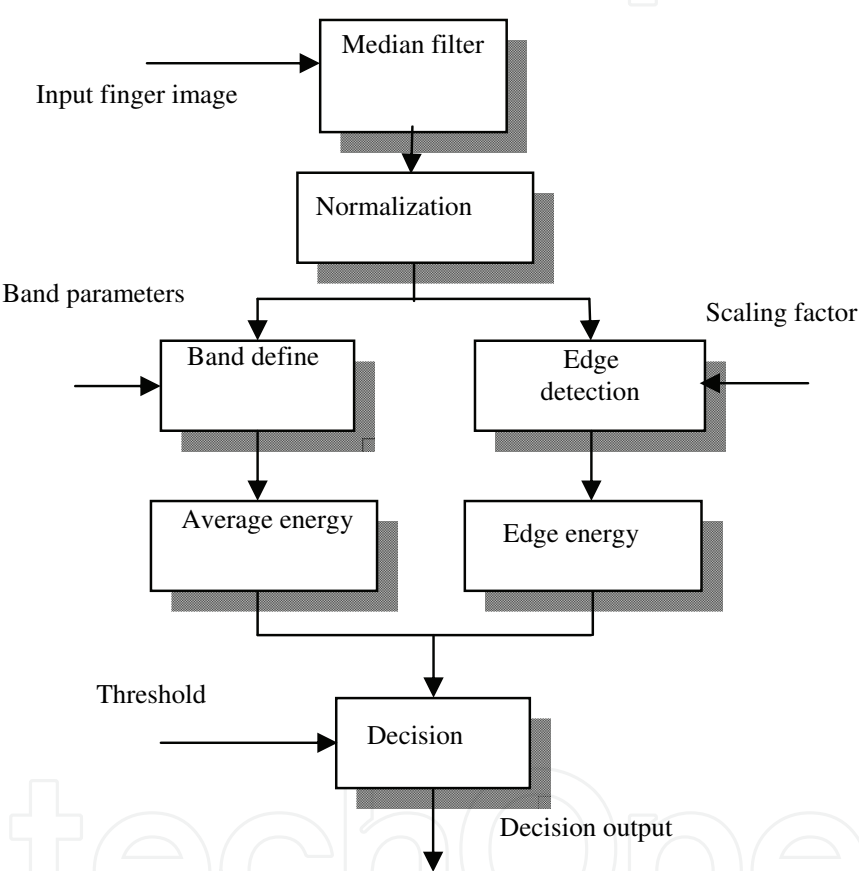


Fig. 23. Image processing flowchart



Fig. 24. Banded image of a real finger at 550nm wavelength with a band width of 300 pixels.

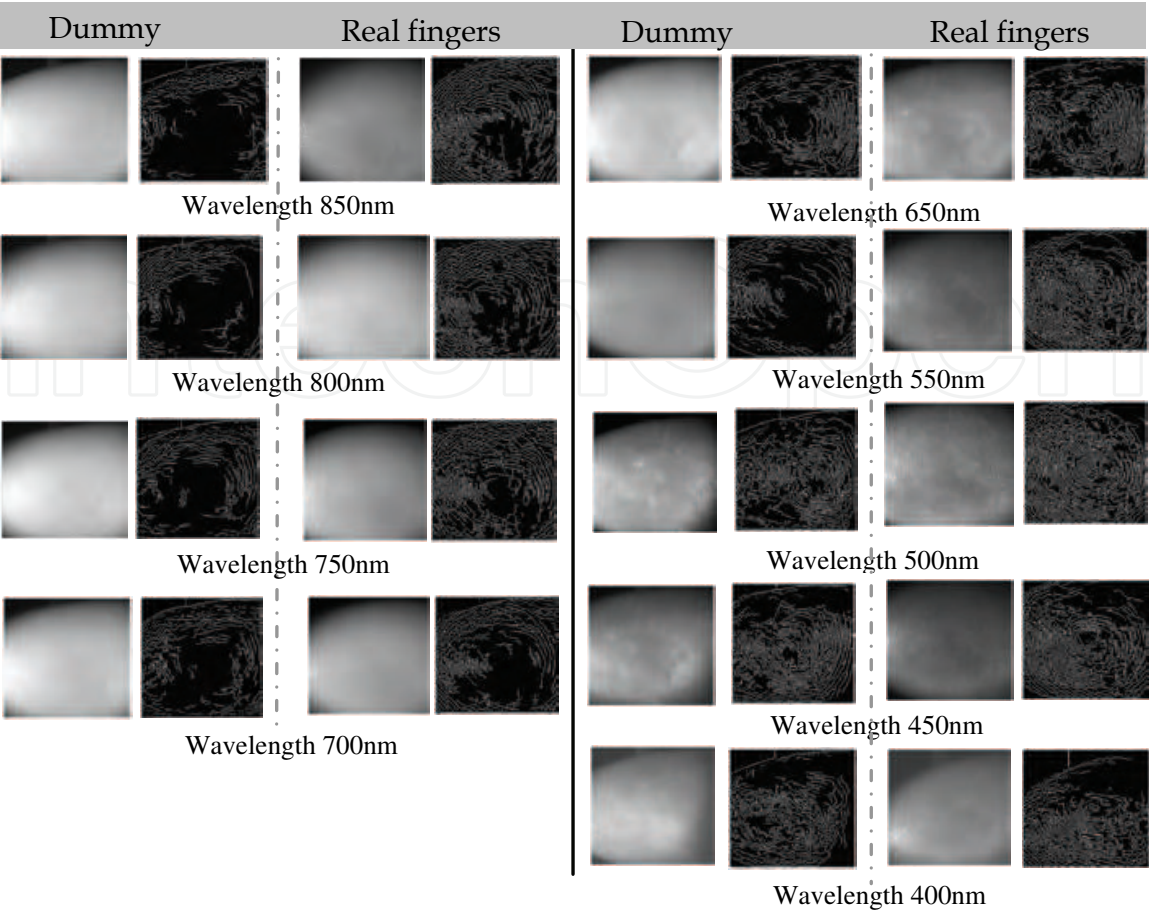


Fig. 25. Finger and finger edge images from dummy and real fingers.

Given the analysis above, the image energy and edge information at NIR wavelengths, (e.g. 850nm), can be used for discriminating between fake and real fingers. Considering that the energy is mostly distributed in the central area of the finger, it is advantageous to setup a banded area to collect the energy as shown in Figure 24.

Table 2 lists the values of average energy (AE) extracted from six fingers at nine wavelengths. Table 3 shows all the values of edge energy (EE) extracted from the same six

Fake	3.27	3.28	3.53	3.42	4.69	4.76	4.95	4.76	4.71
RM1	2.47	2.19	3.19	2.56	3.59	3.76	4.00	4.59	3.32
RM2	2.65	2.98	2.37	2.33	3.70	3.27	3.67	1.99	3.95
RM3	3.81	3.14	3.89	3.47	4.14	4.41	3.95	3.95	4.24
RM4	2.35	2.83	4.01	3.74	5.03	4.58	4.71	4.78	3.76
RF1	4.30	4.11	4.36	4.25	4.77	4.83	4.74	3.44	3.86
RF2	3.08	2.65	2.64	2.59	2.78	3.04	2.82	3.14	3.22
λ(nm)	400	450	500	550	650	700	750	800	850

- Fake: fake finger, modeled from real male finger, RM1. • RM1: real male finger #1. Asian male.
- RM2: real male finger #2. Asian male. • RM3: real male finger #3. White male.
- RM4: real male finger #4. Black male. • RF1: real female finger #1. Asian female.
- RF2: real female finger #2. White female.

Table 2. Average energies (AE values x10<sup>4</sup>) from finger images.



fingers at nine wavelengths. These data show that at the longer wavelengths, particularly at 850 nm, the energy in the fake-finger image is higher than those of real fingers. However, at the shorter wavelengths, there is no clear difference between fake and real ones.

Fake	10.00	12.71	12.39	12.68	9.61	7.05	6.96	5.81	5.19
RM1	10.50	13.31	17.02	14.83	7.24	8.43	11.74	11.53	12.11
RM2	9.41	13.43	13.40	13.88	8.93	9.52	9.42	7.66	10.90
RM3	13.75	13.43	14.90	14.92	9.61	9.33	9.16	10.04	10.74
RM4	9.51	14.62	14.84	14.57	13.47	9.26	8.84	11.50	12.20
RF1	12.35	11.90	11.99	11.83	9.45	11.08	10.93	10.48	10.60
RF2	14.49	12.80	12.64	12.57	7.30	7.76	5.95	7.13	8.08
$\lambda(\text{nm})$	400	450	500	550	650	700	750	800	850

Table 3. Edge energies (EE values  $\times 10^{-2}$ ) from finger edge images.

4.3 Distinguishing artificial fingers from real ones

From the analysis in last section, we see that the ability to discriminate real fingers from fake ones is proportional to the average energy of the finger image, particularly in the longer wavelength band. However, the ability to discriminate is inversely proportional to the average energy of the finger-edge image, again particularly in the longer wavelength band.

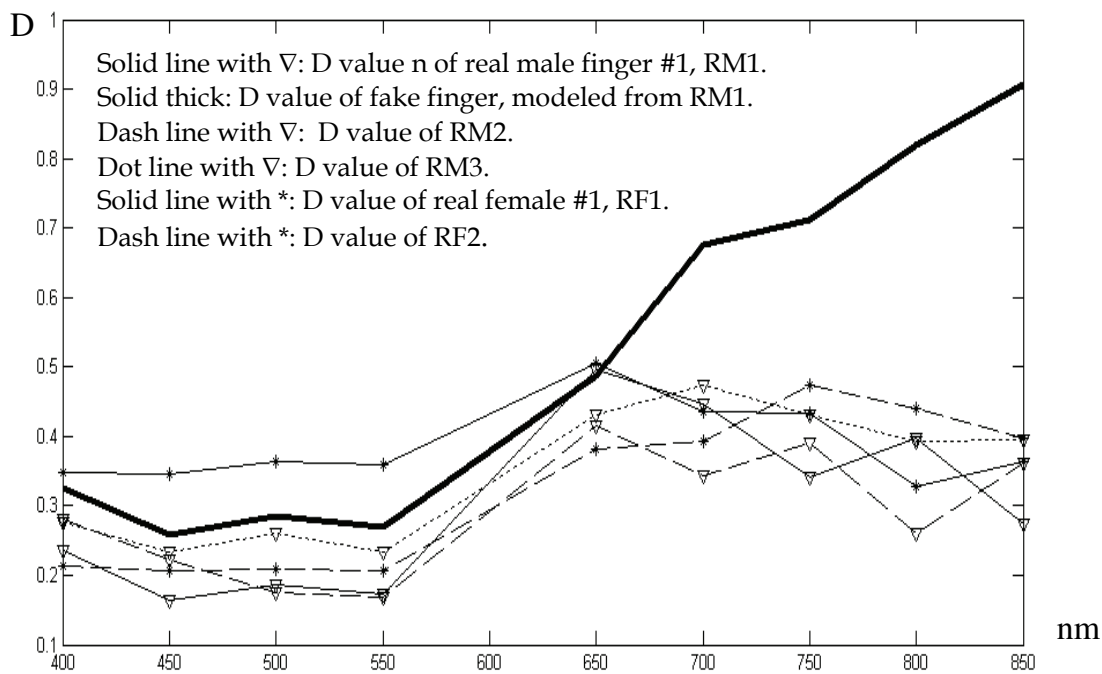


Fig. 26. Decision values for all finger images

Therefore, the decision function for distinguishing artificial fingers from real ones can be constructed using the following equations:

$$F = \begin{cases} 1 & \text{Fake, if } D \geq T \\ 0 & \text{Real, if } D < T \end{cases} \quad (11)$$

where  $D$  is the discrimination value, given by:

$$D = AE / EE \quad (12)$$

The  $D$  values calculated from Table 3 are plotted in Figure 26. From our experiments, we can clearly distinguish the artificial fingers from all the real fingers by setting a threshold value of  $T = 0.55$  at a wavelength of 800nm or 850 nm.

Although the number of testing samples is relatively small, they represent different races. In fact, such a multiple wavelengths database obtained from same living fingers does not exist at the time being. However, the experimental result clearly shows a trend, which demonstrates that as the wavelengths become longer, the fake one gradually separates itself from other real ones, which agrees with the analysis described in earlier sessions.

## 5. Summary and conclusions

In this chapter, we have described several approaches to fingerprint anti-spoofing by means of internal biometrics. Two different methods using NIR optical imaging technology to detect a fake finger are introduced and discussed: 1) optical coherence tomography and, 2) fingerprint NIR image analysis.

Optical coherence tomography provides a powerful new tool for applications in security and document identification. By extending the existing biometric techniques that are based on surface scans of external features, the OCT system can probe and extract the internal features of multilayered objects and tissues. This will be more robust against tampering and counterfeiting. We have demonstrated that OCT techniques can be successfully applied for detecting artificial materials that are commonly used to make fraudulent fingerprints. Overall, the results demonstrate that: 1) Current commercial fingerprint systems have security vulnerabilities and can easily be spoofed by fingerprint dummies; 2) High-resolution 2D OCT images and the corresponding signal curves can clearly reveal the artificial materials; 3) OCT is capable of providing high-resolution 3D images for security identification reference.

Our future research will be focused on increasing the OCT 3D-image acquisition rate, and on applying the current pattern recognition method in processing OCT images (2D and 3D). This will allow systems to better distinguish the artificial fingerprint layer in order to resist spoofing attacks, thereby enhancing the security provided by these applications. However, the cost of such an OCT system is relatively high: the primary component is the broadband IR light source, which can cost thousands of dollars.

In this chapter, we have also described a relatively cheap and practical approach for distinguishing dummy fingers from real ones. The proposed method is based on using the observed spectral features of the sample fingers; experimental testing has shown that near-infrared light can be used to successfully detect differences in the optical properties between real fingers and an artificial one. The artificial finger exhibits back-reflected and scattered light from the deeper structures at NIR wavelengths, whereas real *in vivo* human tissue can absorb more light. The strong back-scattered light from fake finger washes out the surface structure information, thereby blurring the fingerprint ridges.

A simple algorithm based on overall energy and edge energy can be used to identify real fingers from fake ones. The ability to discriminate may improve when using longer wavelengths (e.g., >800 nm), although the use of IR camera will be very expensive. As most of the cameras using the visual band provide some sensing capability at 850 nm, these can be used to create a cost-efficient fingerprint recognition system. Although we used a mercury arc lamp as the light source in the proposed setup, a very cheap but powerful halogen bulb can also serve the same purpose.

This novel method for discriminating between real and dummy fingers is simple, low-cost, and effective. Such a system can be fabricated as a stand-alone detection device, or it can be easily integrated into an existing fingerprint recognition system for the purpose of pre-screening fingers to defeat spoofing.

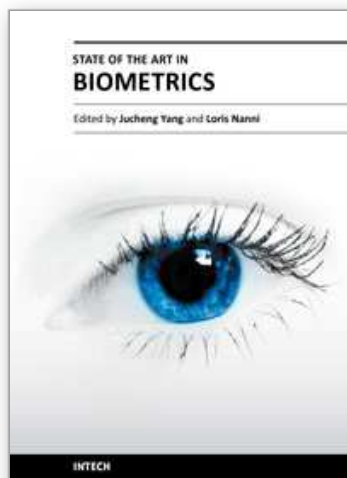
## 6. References

- Akiba M, & Chan KP. (2007). *In vivo* video-rate cellular-level full-field optical coherence tomography. *J Biomed Opt* 12:064024.
- Bashkansky M, Lewis D, Pujari V, Reintjes J, & Yu HY. (2001). Subsurface detection and characterization of Hertzian cracks in Si<sub>3</sub>N<sub>4</sub> balls using optical coherence tomography. *Ndt & E International* 34:547-55.
- Chang S, Cheng Y, Larin KV, Mao Y, Sherif S, & Flueraru C. (2008). Optical coherence tomography used for security and fingerprint-sensing applications. *IET Image Processing* 2:48-58.
- Chang S, Liu XP, Cai XY, & Grover CP. (2005). Full-field optical coherence tomography and its application to multiple-layer 2D information retrieving. *Optics Communications* 246:579-85.
- Chang S, Cai XY, & Flueraru C. (2006a). Image enhancement for multilayer information retrieval by using full-field optical coherence tomography. *Applied Optics* 45:5967-75.
- Chang S, Mao YX, Sherif S, & Flueraru C. (2006b). Full-field optical coherence tomography used for security and document identity - art. no. 64020Q. *Optics and Photonics for Counterterrorism and Crime Fighting II* 6402:Q4020-Q.
- Cheng Y, & Larin KV. (2006). Artificial fingerprint recognition using optical coherence tomography with autocorrelation analysis. *Applied Optics* 45 (cover paper):9238-45.
- Cheng Y, & Larin KV. (2007). *In vivo* Two- and Three-Dimensional Imaging of Artificial and Real Fingerprints with Optical Coherence Tomography. *Photonics Technology Letters* 19:1634-6.
- Chinn SR, & Swanson EA. (1996). Multilayer optical storage by low-coherence reflectometry. *Optics Letters* 21:899-901.
- Dubois A, Vabre L, Boccara AC, & Beaurepaire E. (2002). High-resolution full-field optical coherence tomography with a Linnik microscope. *Applied Optics* 41:805-12.
- Dunkers JP, Parnas RS, Zimba CG, Peterson RC, Flynn KM, Fujimoto JG, & Bouma BE. (1999). Optical coherence tomography of glass reinforced polymer composites. *Composites Part a-Applied Science and Manufacturing* 30:139-45.
- Huang D, Swanson EA, Lin CP, Schuman JS, Stinson WG, Chang W, Hee MR, Flotte T, Gregory K, Puliafito CA, & Fujimoto JG. (1991). Optical Coherence Tomography. *Science* 254:1178-81.

- Liang H, Cid M, Cucu R, Dobre G, Podoleanu A, Pedro J, & Saunders D. (2005). En-face optical coherence tomography - a novel application of non-invasive imaging to art conservation. *Optics Express* 13:6133-44.
- Manapuram RK, Ghosn M, & Larin KV. (2006). Identification of Artificial Fingerprints Using Optical Coherence Tomography Technique *Asian Journal of Physics* 15:15-27.
- Nanni L, & Lumini A. (2009) Descriptors for image-based fingerprint matchers, *Expert Systems with Applications*, 36(10):12414-22.
- Netter FH. (1997). *Atlas of Human Anatomy*. Novartis, East Hanover
- Nixon KA, Aimale V, & Rowe RK. (2008). Spoof Detection Schemes. In *Handbook of Biometrics*: Springer Science + Business Media, L.L.C.
- Rie ER. (1987). The influence of varnishes on the appearance of paintings. *Studies on Conservation* 32:1-13.
- Smolka G. (2008). Optical Coherence Tomography: Technology, Markets, and Applications 2008-2012. *BioOptics World*
- Spring m, Liang H, Peric B, Saunders D, & Podoleanu A. (2008). Optical coherence tomography – a tool for high resolution non-invasive 3D-imaging of the subsurface structure of paintings. In *ICOM Committee For Conservation Newsletter*, pp. 633-40
- Szkułmowska A, Gora M, & Targowska M. (2005) of Conference. The applicability of optical coherence tomography at 1.55  $\mu\text{m}$  to the examination of oil paintings. *6th International Congress on Lasers in the Conservation of Artworks (LACONA VI '05)*. Vienna, Austria
- Szkułmowskaki A, Gora M, Targowska M, Rouba B, Stifter D, & Targow EBP. (2007). *Lasers in the Conservation of Artworks*. New York: Springer Science + Business Media
- Targowski P, Gora M, & Wojtkowski M. (2006). Coherence Tomography for Artwork Diagnostics. *Laser Chemistry*
- Targowski P, Rouba B, Wojtkowski M, & Kowalczyk A. (2004). The application of optical coherence tomography to nondestructive examination of museum objects. *Studies on Conservation* 49:107-14.
- Tuchin VV. (2000). *Tissue Optics: Light Scattering Methods and Instruments for Medical Diagnosis*. Bellingham, WA: SPIE
- Tuchin VV. (2007). *Tissue optics : light scattering methods and instruments for medical diagnosis*. Bellingham, Washington: SPIE Press
- Tuchin VV, Maksimova IL, Zimnyakov DA, Kon IL, Mavlyutov AH, & Mishin AA. (1997). Light propagation in tissues with controlled optical properties. *J Biomed Opt* 2:401-17.
- Tuchin VV, Xu XQ, & Wang RK. (2002). Dynamic optical coherence tomography in studies of optical clearing, sedimentation, and aggregation of immersed blood. *Applied Optics* 41:258.
- Wiesauer K, Pircher M, Gotzinger E, Bauer S, Engelke R, Ahrens G, Grutzner G, Hitzenberger CK, & Stifter D. (2005). En-face scanning optical coherence tomography with ultra-high resolution for material investigation. *Optics Express* 13:1015-24.
- Xiao Q, & Raffat H. (1990). Combining statistical and structural information for fingerprint image processing, classification and identification. In *Pattern recognition: architectures, algorithms and applications*, ed. R Plamondon, H Cheng. Singapore: World Scientific Publishing Co.
- Yan P. & Bowyer, K. W. Biometric Recognition Using Three-Dimensional Ear Shape. <http://www.cse.nd.edu/Reports/2006/TR-2006-01.pdf>



- Yang H, Xie, S., Li, H., and Lu, Z. (2007). Determination of human skin optical properties in vivo from reflectance spectroscopic measurements. *Chinese Optics Letters* 5:181-3.
- Yang JC, & Park DS. (2008). A fingerprint verification algorithm using tessellated invariant moment features, *Neurocomputing* 71:1939-46.
- Zimnyakov DA, Agafonov DN, Sviridov AP, Omel'chenko AI, Kuznetsova LV, & Bagratashvili VN. (2002). Speckle-contrast monitoring of tissue thermal modification. *Appl Opt* 41:5989-96.
- Zimnyakov DA, Ryabukho VP, & Larin KV. (1994). Microlens Effect Due to the Diffraction of Focused Beams on Large-Scale Phase Screens. *Letters to Journal of Theoretical Physics* 20:14.



## **State of the art in Biometrics**

Edited by Dr. Jucheng Yang

ISBN 978-953-307-489-4

Hard cover, 314 pages

**Publisher** InTech

**Published online** 27, July, 2011

**Published in print edition** July, 2011

Biometric recognition is one of the most widely studied problems in computer science. The use of biometrics techniques, such as face, fingerprints, iris and ears is a solution for obtaining a secure personal identification. However, the “old” biometrics identification techniques are out of date. This goal of this book is to provide the reader with the most up to date research performed in biometric recognition and describe some novel methods of biometrics, emphasis on the state of the art skills. The book consists of 15 chapters, each focusing on a most up to date issue. The chapters are divided into five sections- fingerprint recognition, face recognition, iris recognition, other biometrics and biometrics security. The book was reviewed by editors Dr. Jucheng Yang and Dr. Loris Nanni. We deeply appreciate the efforts of our guest editors: Dr. Girija Chetty, Dr. Norman Poh, Dr. Jianjiang Feng, Dr. Dongsun Park and Dr. Sook Yoon, as well as a number of anonymous reviewers

### **How to reference**

In order to correctly reference this scholarly work, feel free to copy and paste the following:

Shoude Chang, Kirill Larin, Youxin Mao, Wahab Almuhtadi and Costel Flueraru (2011). Fingerprint Spoof Detection By NIR Optical Analysis, State of the art in Biometrics, Dr. Jucheng Yang (Ed.), ISBN: 978-953-307-489-4, InTech, Available from: <http://www.intechopen.com/books/state-of-the-art-in-biometrics/fingerprint-spoof-detection-by-nir-optical-analysis>

**INTECH**  
open science | open minds

### **InTech Europe**

University Campus STeP Ri  
Slavka Krautzeka 83/A  
51000 Rijeka, Croatia  
Phone: +385 (51) 770 447  
Fax: +385 (51) 686 166  
[www.intechopen.com](http://www.intechopen.com)

### **InTech China**

Unit 405, Office Block, Hotel Equatorial Shanghai  
No.65, Yan An Road (West), Shanghai, 200040, China  
中国上海市延安西路65号上海国际贵都大饭店办公楼405单元  
Phone: +86-21-62489820  
Fax: +86-21-62489821

© 2011 The Author(s). Licensee IntechOpen. This chapter is distributed under the terms of the [Creative Commons Attribution-NonCommercial-ShareAlike-3.0 License](https://creativecommons.org/licenses/by-nc-sa/3.0/), which permits use, distribution and reproduction for non-commercial purposes, provided the original is properly cited and derivative works building on this content are distributed under the same license.

IntechOpen

IntechOpen